

1 **Deep learned process parameterizations provide better representations of turbulent**  
2 **heat fluxes in hydrologic models**

3 **Enter authors here: Andrew Bennett<sup>1</sup>, Bart Nijssen<sup>1</sup>**

4 <sup>1</sup>Department of Civil and Environmental Engineering, University of Washington, Seattle, WA,  
5 USA

6 Corresponding author: Andrew Bennett ([andrbenn@uw.edu](mailto:andrbenn@uw.edu))

7 **Key Points:**

- 8 • Deep learned process parameterizations of turbulent heat fluxes outperform physically-  
9 based parameterizations.
- 10 • Deep learned process parameterizations can be dynamically coupled into process-based  
11 hydrologic models.
- 12 • Incorporation of process-based model derived states into deep learning introduces  
13 feedbacks that improve long-term simulations.  
14

## 15 **Abstract**

16 Deep learning (DL) methods have shown great promise for accurately predicting hydrologic  
17 processes but have not yet reached the complexity of traditional process-based hydrologic  
18 models (PBHM) in terms of representing the entire hydrologic cycle. The ability of PBHMs to  
19 simulate the hydrologic cycle makes them useful for a wide range of modeling and simulation  
20 tasks, for which DL methods have not yet been adapted. We argue that we can take advantage of  
21 each of these approaches by embedding DL methods into PBHMs to represent individual  
22 processes. We demonstrate that this is viable by developing DL-based representations of  
23 turbulent heat fluxes and coupling them into the Structure for Unifying Multiple Modeling  
24 Alternatives (SUMMA), a modular PBHM modeling framework. We developed two DL  
25 parameterizations and integrated them into SUMMA, resulting in a one-way coupled  
26 implementation (NN1W) which relies only on model inputs and a two-way coupled  
27 implementation (NN2W), which also incorporates SUMMA-derived model states. Our results  
28 demonstrate that the DL parameterizations are able to outperform calibrated standalone SUMMA  
29 benchmark simulations. Further we demonstrate that the two-way coupling can simulate the  
30 long-term latent heat flux better than the standalone benchmark and one-way coupled  
31 configuration. This shows that DL methods can benefit from PBHM information, and the  
32 synergy between these modeling approaches is superior to either approach individually.

## 33 **Plain Language Summary**

34 Machine learning (ML) and process-based methods are two approaches to hydrologic modeling.  
35 Process-based hydrologic models (PBHMs) represent the hydrologic cycle by solving equations  
36 which have been developed from physical theory or experimentation, while ML models make  
37 predictions based on patterns learned from large amounts of data. A particular sub-field of  
38 machine learning called deep learning (DL) has been shown to often outperform process-based  
39 models. However, current DL models do not represent all aspects of the hydrologic cycle (such  
40 as streamflow, evaporation, groundwater storage, and snowpack) at once, as is often done in  
41 PBHMs. As a result, DL models in hydrology are often single purpose, while PBHMs can be  
42 used for many different scientific and/or engineering purposes.

43 We show how individual DL models that simulate evaporation and convective heat transport at  
44 the land surface can be incorporated into a PBHM. We show that deep learning simulated  
45 evaporation and convective heat transport better than the PBHM. We also show how the  
46 incorporation of deep learning into process-based models can further improve the DL model  
47 itself. We conclude that taking advantage of both modeling perspectives is better than either on  
48 its own.

## 49 **1 Introduction**

50 The debates amongst the hydrologic modeling community about the use and utility of machine  
51 learning (ML) to simulate hydrologic processes indicate that much work remains to be done to  
52 understand the role and potential of machine learning in hydrologic modeling (Nearing et al.,  
53 2020; Shen, 2018). While it is true that deep learning (DL) models have shown great promise  
54 and superior performance in many cases it is yet unclear how to make models that are both  
55 composable (that is, easy to combine with other models) and transferable for scientific studies  
56 (that is, the same model configuration can be used to explore disparate scientific questions). In  
57 this paper we outline an approach for coupling DL models of individual processes into existing

58 hydrologic modeling frameworks. This coupling approach allows us to represent individual  
59 physical processes within a larger model using ML methods and to introduce feedbacks between  
60 model components. The ability to couple model components will address these composability  
61 and transferability questions, as well as allow use of these types of machine-learned models in  
62 areas which do not have readily available training data.

63 There are several reasons for the rapid advancement of ML-based approaches in hydrology (and  
64 other fields), including a greater abundance of publicly available data, increased computational  
65 resources, and better frameworks for selecting, fitting, and applying models. Along with this  
66 increase in interest, the community has also begun to think about how to incorporate aspects of  
67 physical theory into these data driven models. This desire for physics-based machine learning is  
68 enticing for a number of reasons. As scientists we hope that the use of models which are based  
69 in, or constrained by, physical properties will allow us to learn about the underlying processes of  
70 the systems we are modeling. Not only that, we hope that such approaches will be able to  
71 efficiently extract information from a variety of datasets, from in situ observations to satellite  
72 remote sensing data, or be able to represent complex phenomena in a more efficient way.

73 While inclusion of empirical or statistical relationships of individual processes in hydrologic  
74 models is common, this is not yet the case for ML methods. One reason for this is that it is not  
75 clear how to combine ML models in the same way that we have been able to include processes  
76 for which we have parsimonious descriptions. Additionally, methodologies for representing  
77 physical relationships between ML-based process representations have not been developed in the  
78 hydrology community. In part, this is not surprising since machine learning is good at resolving  
79 relationships that we have not been able to decompose into easily describable parts. This “whole-  
80 system” or “black box” approach is conceptually appealing due to its simplicity, and is  
81 exemplified by rainfall-runoff modeling, which deep learning has proven to be very good at (Hu  
82 et al., 2018; Kratzert et al., 2018; Moshe et al., 2020). However, by taking a more granular  
83 approach, we will show that DL models can be successfully incorporated as process modules  
84 into existing models. Doing so allows us to see how changes in a single component affect the  
85 entire system.

86 In this paper, we look at turbulent heat fluxes, for which high-quality, long-term, local  
87 observations from eddy covariance towers (here, from FluxNet; Pastorello et al., 2020) are  
88 available across a range of hydroclimates. While machine learning has been used for modeling of  
89 turbulent heat fluxes and evaporation (Jung et al., 2009; Tramontana et al., 2016; Zhao et al.,  
90 2019) there have not yet been model intercomparisons with land surface models, much less  
91 integrations into land surface models. However, Best et al. (2015) showed that even simple  
92 statistical models are often able to outperform state of the art land surface models in simulation  
93 of latent and sensible heat fluxes. Best et al. (2015) postulated that the statistical models were  
94 better able to use the information in the meteorological forcing data than the physics-based  
95 approaches. This indicates there is strong motivation for incorporating data-driven techniques  
96 into complex land surface and hydrologic models. We believe that if these types of approaches  
97 are able to provide better performance than the physically motivated relationships we should  
98 work to understand how and why this performance is better and use them where appropriate and  
99 applicable.

100 Despite the statistical benchmarks’ superior ability for predicting turbulent heat fluxes in Best et  
101 al. (2015), land surface models remain more suitable for a wide range of applications, because

102 they represent a wider range of hydrologic processes and may be better suited for studies of  
103 environmental change. Such studies include drought prediction (Li et al., 2012), snow melt  
104 predictions under climate change (Musselman et al., 2017), and predicting volatile organic  
105 compound emissions (Lathière et al., 2006). That is not to say that ML models cannot be used in  
106 this way or incorporated into larger frameworks. Both Kratzert et al. (2018) and Jiang et al.  
107 (2020) make qualitative comparisons of internal ML model states to snowpack, but do not later  
108 use the models for prediction of snowpack. We believe that it is likely that ML models will be  
109 used for such purposes in the near future, but the question remains open how to extract process  
110 information from statistical models.

111 Because the hydrology community is still learning the best ways to build and use ML models,  
112 there remains considerable room for incorporation of machine learning into more conventional  
113 process-based hydrologic models (PBHMs), which have the flexibility needed for general  
114 purpose modeling. This approach has been adopted recently by Brenowitz & Bretherton (2018)  
115 as well as Rasp et al. (2018) for parameterizing sub-gridcell scale processes, such as cloud  
116 convection, in atmospheric circulation models. Similarly, in oceanography, neural networks have  
117 been used to parameterize the turbulent vertical mixing in the ocean surface (Ramadhan et al.,  
118 2020).

119 In this study, we demonstrate how coupling ML models into a hydrologic model can yield better  
120 performance at estimating turbulent heat fluxes without sacrificing mass and energy balance  
121 closure or the ability to represent other processes such as runoff or snowpack. We have  
122 developed two ML models to simulate latent and sensible heat fluxes. We embed these ML  
123 models as process parameterizations inside of a PBHM. These ML-based process  
124 parameterizations replace the turbulent heat flux equations of the original PBHM. Our first  
125 model was only allowed to learn from the same meteorological data that is used to force the  
126 hydrologic model, while our second ML model is additionally trained with the inclusion of states  
127 derived from the hydrologic model. We show that both ML models are able to outperform the  
128 routines for simulating turbulent heat fluxes at subdaily timescales. We also show that the  
129 configuration which was trained using model states is better able to reproduce the long-term  
130 water balance. Our results indicate that approaches to coupling machine learning with PBHMs  
131 offer a promising avenue, which has only begun to be explored.

## 132 **2 Materials and Methods**

### 133 2.1 Data and study sites

134 We used data from 60 FluxNet sites (Pastorello et al., 2020) to run our experiments. These sites  
135 cover a large variety of vegetation and climate classifications. Our site selection process  
136 considered several criteria. We first filtered the full FluxNet dataset to make sure we only  
137 included sites which had energy balance corrected measurements of both sensible and latent heat  
138 fluxes, which will be discussed later. We then made sure that these sites had the necessary  
139 variables to force our models, which include precipitation, air temperature, incoming shortwave  
140 radiation, incoming longwave radiation, specific humidity, air pressure, and wind speed. We then  
141 removed sites which had either fewer than three years of contiguous data or more than 20%  
142 missing observations during the longest continuous period with observations. For the remaining  
143 sites, we used gap-filled data provided as part of the FluxNet dataset. Gap-filling was based on  
144 ERA-Interim (ERA-Interim) (Dee et al., 2011) and includes downscaling and postprocessing explicitly

145 for the purpose of model forcing. Time steps flagged as gap-filled were excluded from our  
146 performance analysis to ensure that we did not simply measure the ability of our simulations to  
147 model ERAI data. However, the gap-filled data is included when analyzing the water balance.

148 We also limited our analysis to sites which had an observed ET/P ratio of less than 1.1,  
149 calculated using the mean FluxNet-reported values of ET and P over the simulation period. This  
150 was done to accommodate our model structure, which enforces mass and energy balances on a  
151 point (or lumped) scale. Larger observed ET/P ratios likely occur at sites which have strong  
152 spatial gradients and flow convergence, so that moisture available for ET is not just the result of  
153 local precipitation. Our filtering process resulted in 60 sites with 508 site-years of data. A  
154 breakdown of the site names, data periods, locations and site characteristics are given in Table 1.  
155 Figure 1 shows the locations and vegetation classes for these same sites.

156 **Table 1.** A listing of the sites, locations, IGBP vegetation types, and dates of simulation.  
157 Locations are given as (Latitude ( $^{\circ}$ N), Longitude ( $^{\circ}$ E)). Vegetation types are given by their IGBP  
158 codes. MF is mixed forest, ENF is evergreen needleleaf forest, CRL is croplands, GRL is  
159 grasslands, SVN is savannas, OSL is open shrublands, WLD is permanent wetlands, DBF is

160 deciduous broadleaf forest, and WS is woody savannas. Site names are taken from FluxNet, and  
 161 consist of a two-letter country code followed by a three-letter site code.

| Site name | Location       | Veg Type | Start Time | End Time | Site name | Location       | Veg Type | Start Time | End Time |
|-----------|----------------|----------|------------|----------|-----------|----------------|----------|------------|----------|
| AT-Neu    | (47.1, 11.3)   | GRL      | 1-2002     | 12-2012  | FI-Let    | (60.6, 24)     | ENF      | 7-2009     | 12-2012  |
| AU-ASM    | (-22.3, 133.2) | ENF      | 1-2010     | 12-2014  | FI-Sod    | (67.4, 26.6)   | ENF      | 4-2002     | 4-2005   |
| AU-Cpr    | (-34, 140.6)   | SVN      | 1-2010     | 12-2014  | FR-LBr    | (44.7, -0.8)   | ENF      | 1-1996     | 12-2008  |
| AU-DaP    | (-14.1, 131.3) | GRL      | 6-2007     | 12-2013  | FR-Pue    | (43.7, 3.6)    | EBF      | 7-2004     | 3-2013   |
| AU-How    | (-12.5, 131.2) | WS       | 4-2009     | 12-2014  | IT-Cpz    | (41.7, 12.4)   | EBF      | 4-2000     | 1-2009   |
| AU-Stp    | (-17.2, 133.4) | GRL      | 4-2008     | 12-2014  | IT-Lav    | (46, 11.3)     | ENF      | 1-2003     | 12-2014  |
| AU-Wac    | (-37.4, 145.2) | EBF      | 5-2005     | 12-2008  | IT-MBo    | (46, 11)       | GRL      | 1-2003     | 12-2013  |
| AU-Wom    | (-37.4, 144.1) | EBF      | 1-2010     | 12-2014  | IT-Noe    | (40.6, 8.2)    | CSL      | 2-2004     | 12-2014  |
| BE-Lon    | (50.6, 4.7)    | CRL      | 4-2004     | 10-2013  | IT-Ren    | (46.6, 11.4)   | ENF      | 8-2003     | 12-2013  |
| BE-Vie    | (50.3, 6)      | MF       | 1-1996     | 12-2014  | IT-Ro2    | (42.4, 11.9)   | DBF      | 1-2002     | 2-2007   |
| CA-Gro    | (48.2, -82.2)  | MF       | 1-2003     | 12-2014  | IT-SRo    | (43.7, 10.3)   | ENF      | 6-2000     | 4-2009   |
| CA-Qfo    | (49.7, -74.3)  | ENF      | 1-2003     | 12-2010  | IT-Tor    | (45.8, 7.6)    | GRL      | 4-2008     | 12-2014  |
| CA-TP1    | (42.7, -80.6)  | ENF      | 1-2002     | 12-2014  | NL-Hor    | (52.2, 5.1)    | GRL      | 7-2004     | 4-2009   |
| CA-TP3    | (42.7, -80.3)  | ENF      | 1-2002     | 12-2014  | RU-Fyo    | (56.5, 32.9)   | ENF      | 1-1998     | 12-2014  |
| CA-TPD    | (42.6, -80.6)  | DBF      | 1-2012     | 12-2014  | US-AR2    | (36.6, -99.6)  | GRL      | 5-2009     | 12-2012  |
| CH-Cha    | (47.2, 8.4)    | GRL      | 1-2006     | 3-2014   | US-ARM    | (36.6, -97.5)  | CRL      | 1-2003     | 12-2012  |
| CH-Fru    | (47.1, 8.5)    | GRL      | 1-2006     | 2-2014   | US-Blo    | (38.9, -120.6) | ENF      | 5-1998     | 12-2007  |
| CN-HaM    | (37.4, 101.2)  | GRL      | 1-2002     | 12-2004  | US-CRT    | (41.6, -83.3)  | CRL      | 1-2011     | 12-2013  |
| CZ-wet    | (49, 14.8)     | WLD      | 3-2009     | 12-2014  | US-GLE    | (41.4, -106.2) | ENF      | 9-2004     | 12-2014  |
| DE-Geb    | (51.1, 10.9)   | CRL      | 1-2001     | 12-2014  | US-Goo    | (34.3, -89.9)  | GRL      | 5-2002     | 12-2006  |
| DE-Gri    | (51, 13.5)     | GRL      | 1-2004     | 12-2014  | US-IB2    | (41.8, -88.2)  | GRL      | 1-2004     | 12-2011  |
| DE-Hai    | (51.1, 10.5)   | DBF      | 1-2000     | 8-2011   | US-KS2    | (28.6, -80.7)  | CSL      | 5-2003     | 12-2006  |
| DE-Kli    | (50.9, 13.5)   | CRL      | 5-2006     | 12-2014  | US-Los    | (46.1, -90)    | WLD      | 9-2000     | 2-2009   |
| DE-Obe    | (50.8, 13.7)   | ENF      | 1-2008     | 12-2014  | US-NR1    | (40, -105.5)   | ENF      | 1-1998     | 12-2014  |
| DE-Tha    | (51, 13.6)     | ENF      | 1-1996     | 12-2014  | US-Prr    | (65.1, -147.5) | ENF      | 11-2010    | 12-2014  |
| DK-Eng    | (55.7, 12.2)   | GRL      | 6-2005     | 10-2008  | US-Syv    | (46.2, -89.3)  | MF       | 9-2001     | 1-2008   |
| ES-Amo    | (36.8, -2.3)   | OSL      | 6-2007     | 12-2012  | US-Ton    | (38.4, -121)   | WS       | 1-2001     | 12-2014  |
| ES-LJu    | (36.9, -2.8)   | OSL      | 1-2004     | 12-2013  | US-Var    | (38.4, -121)   | GRL      | 11-2000    | 12-2011  |
| FI-Hyy    | (61.8, 24.3)   | ENF      | 10-2004    | 8-2012   | US-WCr    | (45.8, -90.1)  | DBF      | 8-2010     | 12-2014  |
| FI-Jok    | (60.9, 23.5)   | CRL      | 2-2000     | 11-2003  | US-Whs    | (31.7, -110.1) | OSL      | 1-2007     | 12-2014  |

162  
 163 As noted, we chose to use the FluxNet-provided energy balance corrected turbulent heat  
 164 fluxes. The energy balance gap in eddy-covariance measurements is an extensively studied topic  
 165 (Foken, 2008; Kidston et al., 2010; Wilson et al., 2002), though no strong consensus has been  
 166 reached on how to account for gaps in the observed energy balance (or even whether one  
 167 should). However, because we will be using models and methods that enforce energy  
 168 conservation, we chose to use the corrected fluxes provided by the FluxNet data providers  
 169 (Pastorello et al., 2020).

170



171

172 **Figure 1.** A map of the FluxNet sites used in the analysis, coded by the IGBP vegetation type.

173

## 2.2 SUMMA standalone simulations

174 We used the Structure for Unifying Multiple Modeling Alternatives (SUMMA) to simulate the  
 175 hydrologic cycle (Clark et al., 2015) including the resulting turbulent heat fluxes. SUMMA is a  
 176 hydrologic modeling framework that allows users to select between different model  
 177 configurations and process parameterizations. The clean separation between the numerical solver  
 178 and flux parameterizations allowed us to be confident that coupled DL parameterizations  
 179 embedded into SUMMA did not affect any model components in unintentional ways. The core  
 180 numerical solver in SUMMA enforces closure of the mass and energy balance and is used in all  
 181 of our simulations.

182 SUMMA provides multiple flux parameterizations and process representations for many  
 183 hydrologic processes. Because we were primarily interested in turbulent heat fluxes, we used a  
 184 configuration for the other processes which would be suitable for general purpose hydrologic  
 185 modeling, including runoff and snowpack simulations. For simulation of transpiration we used a  
 186 Ball-Berry approach for simulating stomatal conductance (Ball et al., 1987), an exponentially  
 187 decaying root density profile, and soil moisture controls that mimic the Noah land surface model  
 188 (Niu et al., 2011). Similarly, the radiative transfer parameterizations which are the primary  
 189 controls on the sensible heat fluxes are also set up to mimic the Noah land surface model. The  
 190 functional forms of the turbulent heat fluxes in SUMMA is similar to many other land surface  
 191 and hydrologic models, given by the bulk transfer equations (in resistance terms) as in Bonan  
 192 (2015).

193 At each of the sites described in section 2.1 we independently calibrated a standalone SUMMA  
 194 model using the dynamically dimensioned search algorithm (Tolson & Shoemaker, 2007) as  
 195 implemented in the OSTRICH optimization package (Matott, 2017) using the mean squared  
 196 error as the optimization criteria. A summary of the calibration variables and test ranges is shown  
 197 in table S1 of the supporting information. The first year of available data was used for

198 calibration. Because of the limited length of the data record at some sites, the calibration period  
199 was not excluded from subsequent analysis. The 10 parameters we chose to calibrate largely  
200 control water movement through the vegetation and soil domains. In the soil domain these  
201 include the residual and saturated moisture contents, field capacity, and controls on anisotropy of  
202 flows. In the vegetation domain these include controls on photosynthesis, rooting depth, wilting  
203 and transpiration water contents, amount of throughfall of precipitation through the canopy, and  
204 a generic scaling factor for the amount of vegetation.

205 The calibrations were run to a maximum of 500 trial iterations, which provided good  
206 convergence across sites (see the supporting information for convergence plots). We used the  
207 mean square error at a half hourly timestep for both the latent and sensible heat as the objective  
208 function and saved the best set of parameters for each site to use as our comparison to the DL  
209 parameterizations. To provide good estimates of the initial soil moisture and temperature states  
210 we spun up the standalone SUMMA simulations for 10 years both before and after calibration  
211 (for a total of 20 spinup years). We will refer to the standalone calibrated SUMMA simulations  
212 as SA (StandAlone) for the remainder of the paper. To summarize, we independently calibrated a  
213 set of parameters for each site, whose resulting best parameter set was used as an in-sample  
214 benchmark for comparison with our DL parameterizations. A brief description of the  
215 computational cost and runtimes associated with calibrating SA is provided in the supporting  
216 information.

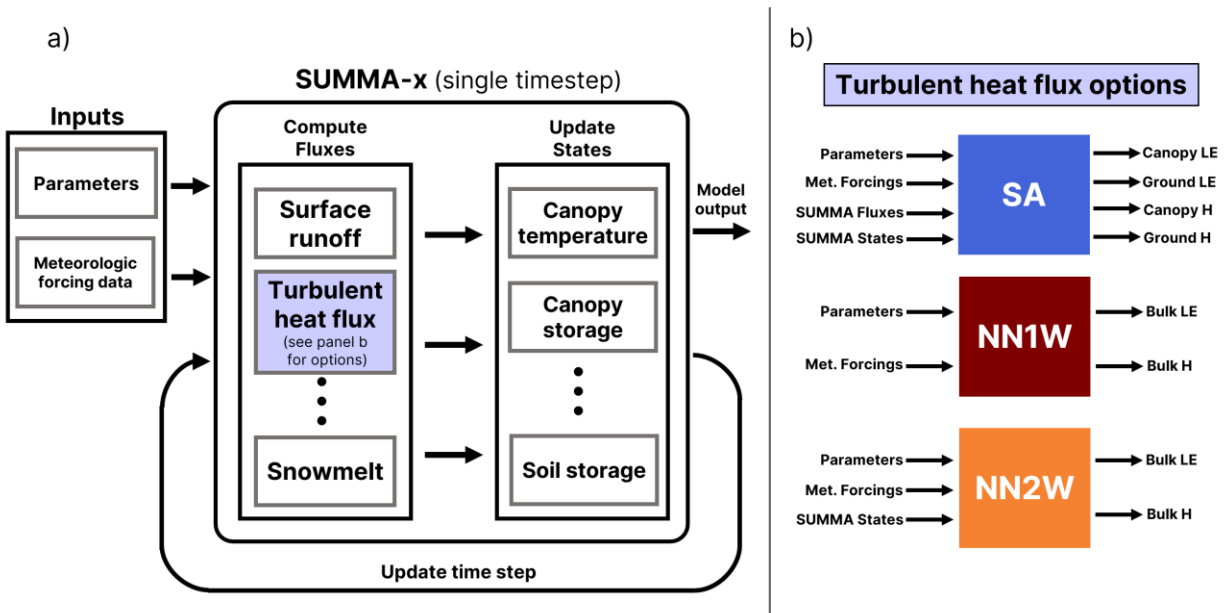
### 217 2.3 DL parameterization and simulations

218 To build DL parameterizations of turbulent heat fluxes we constructed our neural networks using  
219 the Keras python package (Chollet, 2015). The neural networks take in a variety of input data  
220 such as meteorologic forcing data and output the bulk latent and sensible heat fluxes as shown in  
221 panel b) of figure 2.

222 Our neural networks were constructed using only dense layers where every node in one layer is  
223 connected to all nodes in the preceding and following layers. We used the deep-dense  
224 architecture because it is the only network architecture that could easily be coupled to SUMMA,  
225 given the capabilities of the coupling tools. We will discuss the details of how we coupled the  
226 neural networks to SUMMA later in this section. We tested networks with as few as one layer  
227 and 12 nodes and up to 10 layers and 64 nodes were tested. After manual trial and error we  
228 settled on 6 layers each with 48 nodes. Smaller architectures were not as well able to capture the  
229 extremes of the turbulent heat fluxes and larger networks showed diminishing additional  
230 improvement. A simple schematic of the neural network architecture is shown in figure S2 of the  
231 supporting information.

232 We used hyperbolic tangent (tanh) activations in all of the nodes of the network. Stochastic  
233 gradient descent (SGD) with an exponential learning rate decay curve was used as the optimizer  
234 to train the weights and biases of the neural networks. We used the mean square error (the same  
235 as our objective function in the calibration of SA) in the 30-minute turbulent heat flux estimates  
236 as our loss function, similar to the objective function in our calibration of the SUMMA-SA  
237 simulations. Dropout was applied after the first layer and before the final layer with a retention  
238 rate of 0.9 to regularize. Dropout works by randomly pruning some fraction (one minus the  
239 retention rate) of the nodes in a given layer during training. This reduces the likelihood of  
240 overfitting the network as there is some stochasticity in the model architecture during training.

241 When training the networks we performed a 5-fold cross validation. We used 48 sites to train  
 242 each network and then applied it out of sample to each of the remaining 12 sites. The data from  
 243 the 48 sites used to train each network were randomly shuffled and split into 80% training and  
 244 20% validation data. The validation data was used to define an early stopping criterion for the  
 245 training procedure where training was stopped if the validation loss was not decreased for 10  
 246 training epochs. This procedure keeps the model from overfitting on the training data. The  
 247 maximum number of training epochs was set to 500 epochs, with a batch size of 768 data points  
 248 (or 14 days of data points). All data was shuffled before training to remove any temporal bias  
 249 that the model could learn, which also reduces overfitting.



250

251 **Figure 2.** A schematic representation of the model setup. Panel a) shows the SUMMA runtime  
 252 process. Parameters and meteorologic forcing data, as well as the state variables from the  
 253 previous timestep, are fed to SUMMA to compute all fluxes, which are used to update the state  
 254 variables for the subsequent timestep. The purple box labeled “Turbulent heat flux” highlights  
 255 the process representation that we modify in our experiment. Panel b) shows the ways we  
 256 represent the turbulent heat fluxes. One of the options from panel b) replaces the purple box in  
 257 panel a). SA is the standalone SUMMA representation, as described in section 2.2. NN1W and  
 258 NN2W are our DL-based representations described in section 2.3. Thus, SUMMA-x represents  
 259 one of the three model configurations where x is one of SA, NN1W, or NN2W.

260 The first network we trained took meteorological forcing data for the current timestep, vegetation  
 261 and soil types, and the calibrated SUMMA parameter values as input. We chose to include the  
 262 calibration parameters to provide the same information to the neural networks as was provided to  
 263 the calibrations, allowing for a more direct comparison and because the calibrated parameter  
 264 values might be a proxy for site characteristics that can be associated with different responses  
 265 among the sites. The neural network outputs the bulk latent and sensible heat fluxes at the half  
 266 hourly timescale. We denote this network NN1W, for Neural-Network-1-Way, because this  
 267 configuration only takes meteorological forcing data and parameters, which cannot be changed

268 by the rest of the SUMMA calculations. That is, the neural network provides information about  
269 turbulent heat fluxes to SUMMA, but SUMMA does not provide any internally-derived  
270 information to the neural network.

271 The second network we trained took all of the same input data as the NN1W configuration, as  
272 well as a number of additional inputs that are derived states taken from the output of the coupled  
273 SUMMA-NN1W simulations. We included surface vapor pressure, leaf area index, surface soil  
274 layer volumetric water content, depth averaged transpirable water (as a volumetric fraction),  
275 surface soil layer temperature, depth averaged soil temperature, and a snow-presence indicator.  
276 These variables were chosen because they are used in the process-based SUMMA  
277 parameterizations for either latent or sensible heat, or affect the way in which the partitioning of  
278 the heat flux is distributed to the soil, vegetation, or snow domains. At runtime this network uses  
279 the additional variables as calculated internally by SUMMA, rather than the ones provided  
280 during training from NN1W. We denote this network NN2W, for Neural-Network-2-Way,  
281 because SUMMA internal states provide feedback to the ML model. That is, the neural network  
282 is provided inputs which are dependent on the state variables derived internally by SUMMA,  
283 which in turn depend on the turbulent heat fluxes that are predicted by the neural network.

284 After training each of these networks they were saved and translated into a format that could be  
285 loaded into Fortran via the Fortran Keras Bridge (FKB) package (Ott et al., 2020). The FKB  
286 package allows for translation of a limited subset of Keras model files (architecture, weights,  
287 biases, and activation functions) to be translated into a file format which can be loaded into the  
288 FKB Fortran library which implements several simple components for building and evaluating  
289 neural networks in Fortran, such as the deep-dense architecture used here.

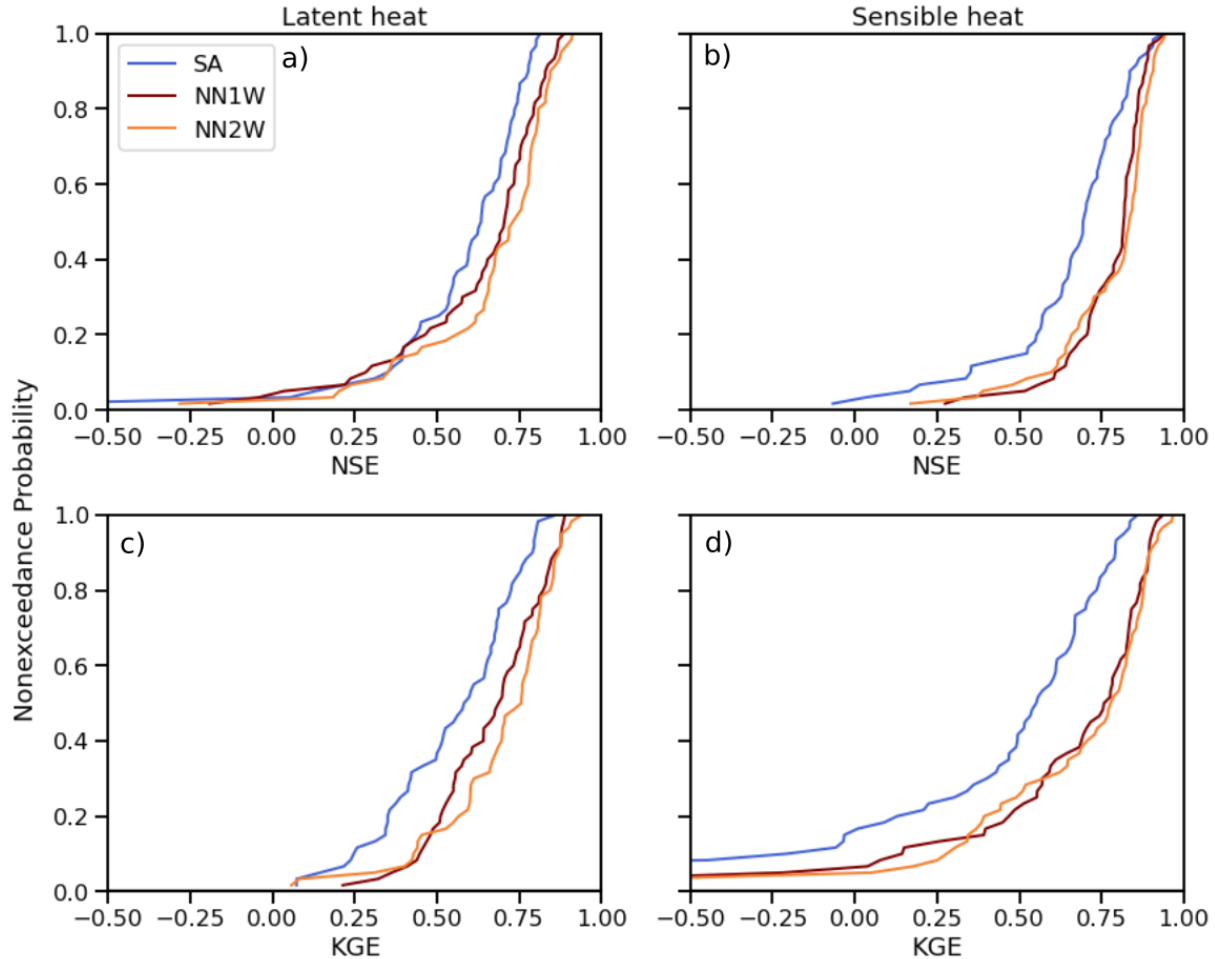
290 We then extended SUMMA (which is written in Fortran) to allow for the use of these neural  
291 networks to simulate the turbulent heat fluxes. Normally SUMMA breaks the calculation of  
292 turbulent heat fluxes into several domains to delineate between heat exchanges in the vegetation  
293 and soil domains. Because we estimate these as bulk quantities we implemented this as only heat  
294 fluxes in the soil domain, and specified that the model should skip any computation of vegetation  
295 fluxes. We then specified that all ET resulting from the neural network's estimate of latent heat  
296 be taken from the soil domain as transpiration, according to SUMMA's internal routines. We  
297 chose this rather than taking all of the ET as soil evaporation because this allowed for a wider  
298 range of ET behaviors. In our simulations, the domain was split into nine soil layers, with a 0.01  
299 m deep top layer. In SUMMA soil evaporation is only taken from the top soil layer and the  
300 shallow surface soil depth in our setup would not have allowed for sufficient storage to satisfy  
301 the predicted ET for many of the vegetated sites. Water removed as transpiration is weighted by  
302 the root density in each soil layer, which generally provides a large enough reservoir to satisfy  
303 the evaporative demand predicted by the neural networks. Another side-effect of our decision for  
304 taking all ET as transpiration is the removal of snow sublimation from the model entirely. As we  
305 will show in the results, the amount of snow sublimation in the SA simulations is negligible at  
306 most of our FluxNet sites, so we believe that this is an acceptable simplification for our initial  
307 demonstration. In cases where the neural network predicts greater evaporation than is available  
308 in the soil SUMMA enforces the water balance and limits the evaporation to an amount it can  
309 satisfy. A brief comparison of the computational cost and runtimes associated with training both  
310 NN1W and NN2W is provided in the supporting information.

### 311 **3 Results**

312 We present our results in two categories. First, we compare the performance of the coupled  
313 neural network simulations to the standalone calibrated simulations (SA). We use two commonly  
314 used metrics for determining the performance of the simulated turbulent heat fluxes, the Nash-  
315 Sutcliffe efficiency (NSE) and Kling-Gupta efficiency (KGE) scores. Using two metrics in  
316 tandem allows us to be sure that our results are robust (Knoben et al., 2019). Then, we explore  
317 how the inclusion of NN-based parameterizations for turbulent heat fluxes affects the overall  
318 model dynamics. This analysis is crucial to ensure that the new parameterizations do not lead to  
319 unrealistic simulations of other processes

#### 320 3.1 Performance analysis

321 Figure 3 shows the cumulative density functions of the performance metrics across all sites,  
322 evaluated on the half-hourly data for all non-gap-filled periods. For all cases we see that both  
323 NN1W and NN2W outperformed the SA simulations. NN1W showed a median increase in NSE  
324 of 0.07 for latent heat and 0.12 for sensible heat, while NN2W showed a median increase in NSE  
325 of 0.10 for latent heat and 0.14 for sensible heat. Similarly, for KGE these were 0.10 (latent) and  
326 0.21 (sensible) for NN1W and 0.17 (latent) and 0.23 (sensible) for NN2W. Examination of the  
327 individual KGE components (bias, variance, and correlation) shows that the NNs showed  
328 consistent improvements in all components. Overall we see that the NN2W configuration  
329 slightly outperforms the NN1W configuration. However, it is possible that in both cases that  
330 there are additional performance gains to be made with better model architectures and/or training  
331 procedures. We will come back to this in the Discussion.



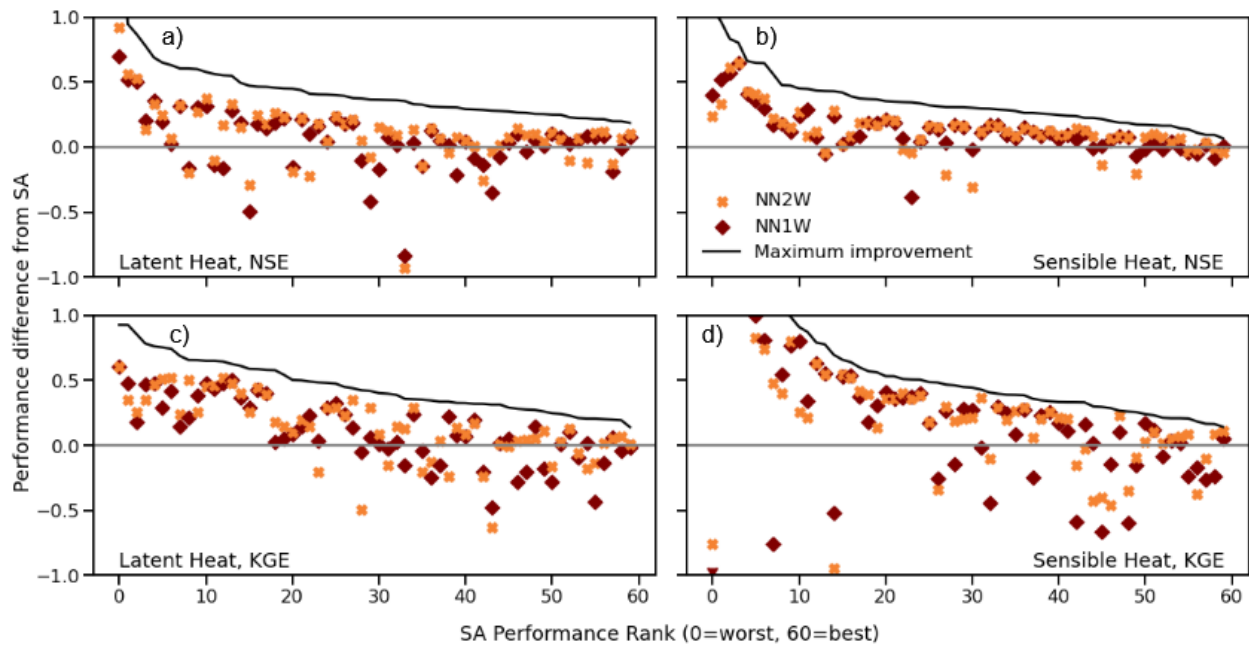
332  
 333 **Figure 3.** Empirical CDFs of performance measures for simulations across all sites. a) shows the  
 334 NSE for latent heat, b) the NSE for sensible heat, c) the KGE for latent heat, and d) the KGE for  
 335 sensible heat.

336  
 337 Even though the curves of the performance measures look quite similar between NN1W and  
 338 NN2W, the performance differences from SA were not always perfectly correlated. Figure 3  
 339 shows the change in performance from SA for each site, ranked by SA performance. The  
 340 maximum improvement that is possible is also shown to provide a reference to account for the  
 341 fact that the range of both NSE and KGE is  $(-\infty, 1]$ . That is, there is more room for improvement  
 342 for poorly performing sites than there is for well performing sites. For both performance  
 343 measures and fluxes the general pattern of improvement follows the maximum improvement  
 344 curve, with some added noise.

345 While on average the NN-based configurations performed better than the SA simulations, they  
 346 performed worse at some locations. NN-based simulations generally had a higher NSE, but the  
 347 KGE scores were more mixed for sensible heat, with SA outperforming the NN-based  
 348 configurations at a number of sites. The NN-based configurations performed much worse at AT-  
 349 Neu, DK-Eng, and CH-Cha (the outliers in the lowest 25th percentile of Figure 4d), where they  
 350 failed in simulating large, upward, nighttime sensible heat fluxes. SA also performed poorly for  
 351 these nighttime fluxes, but to a lesser extent. For latent heat, while some sites showed higher

352 NSE and KGE values for SA results than for the NN-based simulations, more sites showed poor  
 353 performance across all configurations when evaluated by NSE. Decreases in performance  
 354 relative to SA mostly occurred where the NN-based configurations consistently overestimated  
 355 latent heat during winter, which most likely stems from our assumption that all latent heat is  
 356 treated as transpiration. For both conditions for which SA outperformed the NN-based  
 357 configurations, we believe that the performance of the NN-based configurations can be improved  
 358 if more training data or more sophisticated ML methods were used, since the number of outliers  
 359 was small and the average performance improvement was large.

360

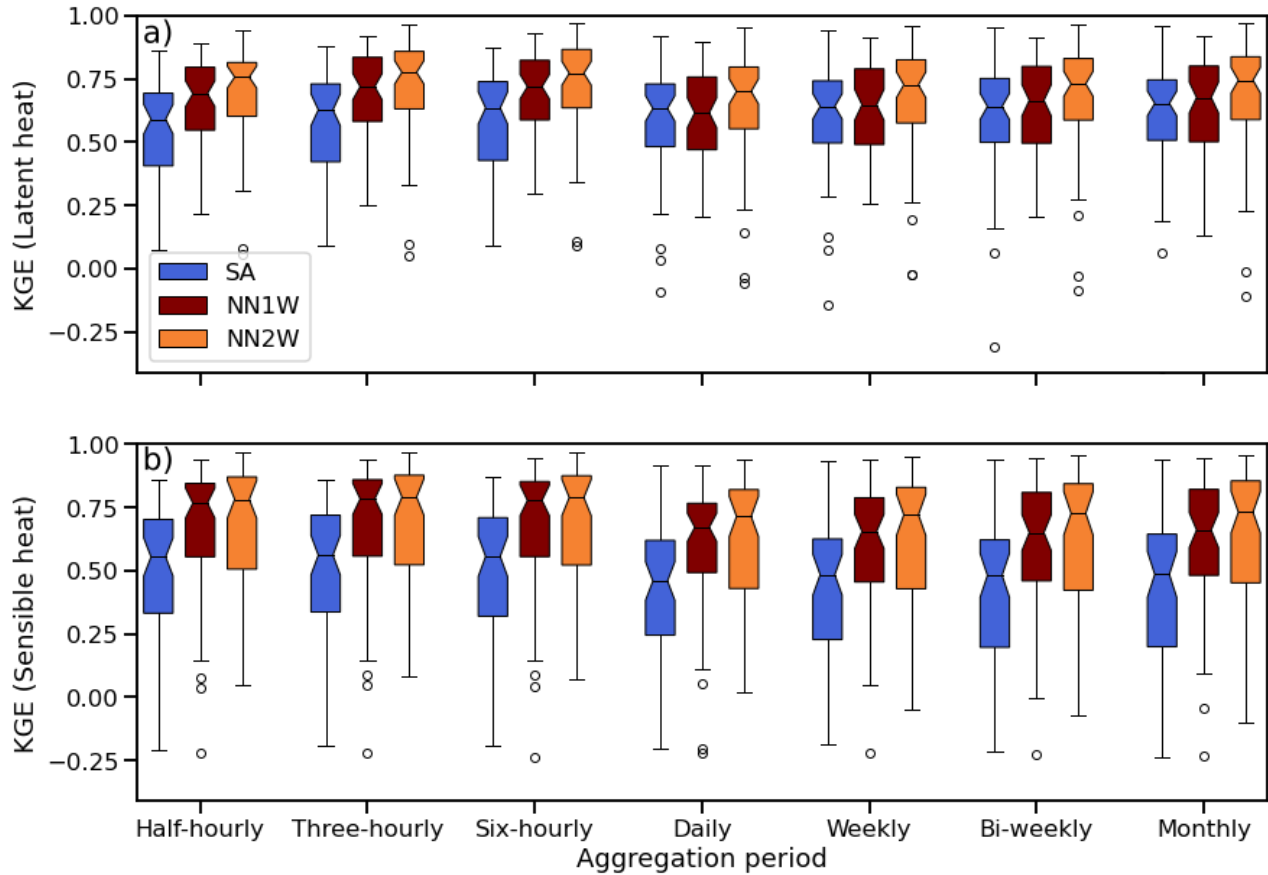


361

362 **Figure 4.** Scatter plots showing the performance of NN1W and NN2W against SA across all  
 363 sites. Points above the grey zero line show configurations where the NN configuration improved  
 364 performance over SA. The “Maximum improvement” line is based on the performance of the SA  
 365 simulations, and is simply  $(1-\text{NSE})$  in subplots a and b, and  $(1-\text{KGE})$  in subplots c and d.

366 We also compared the KGE for different periods of temporal aggregation to evaluate whether  
 367 performance improvements of the NN configurations persisted across timescales (Figure 5). The  
 368 KGE score was chosen here because it shows greater variability than the NSE score in Figure 3,  
 369 though the results are similar for NSE. We see that the sub-daily aggregations, on average,  
 370 showed better performance for both NN configurations, demonstrating that they were able to  
 371 capture the diurnal cycle of turbulent heat fluxes. This is mostly due to the strong dependence of  
 372 turbulent heat fluxes on solar radiation, which we will further explore in section 3.2. Both  
 373 NN1W and NN2W were able to outperform SA across all timescales for sensible heat.

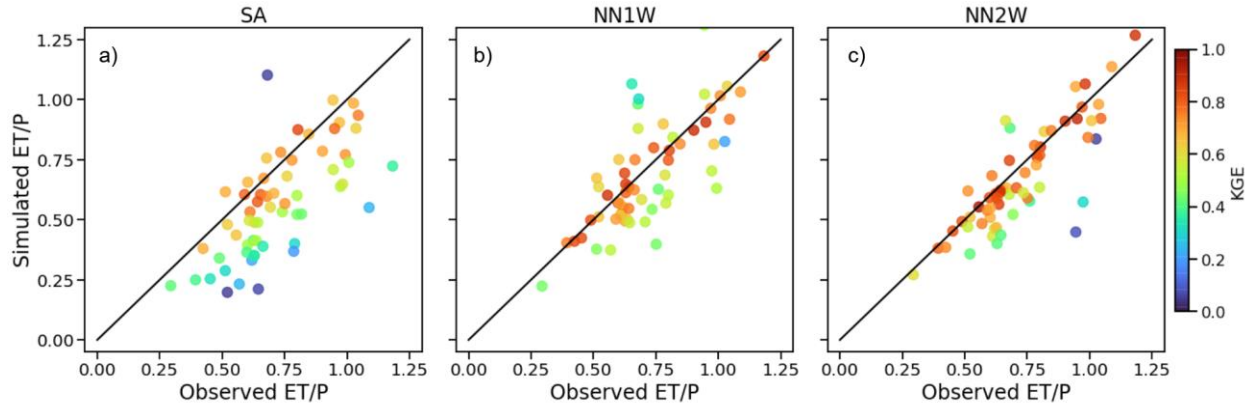
374 However, at daily and longer temporal aggregations differences between models were seen in  
 375 latent heat performance. The NN1W configuration performed better at sub-daily timescales than  
 376 for daily or longer aggregations, for which performance was similar to SA. In contrast, the  
 377 NN2W configuration performed better for latent heat than SA across all timescales.



378  
 379 **Figure 5.** Performance of each model configuration for multiple temporal aggregations. Each  
 380 box shows the interquartile range, with the median marked as the central line. A 95% confidence  
 381 interval for the estimate of the median is represented by the notched portion. Outliers are shown  
 382 as open circles.

### 383 3.2 Diagnostic analysis

384 In section 3.1 we demonstrated that the NN configurations were able to consistently outperform  
 385 the SA configuration for both latent and sensible heat flux predictions at a half-hourly timestep.  
 386 The range of performance differences shown in Figure 4 demonstrates that the NN-based  
 387 simulations are significantly different from the physically-based representation in SA.  
 388 Consequently, water and energy partitioning in the NN configurations is likely much different  
 389 than in SA. To explore the effect of the new NN-based parameterizations on the simulated water  
 390 cycle we first compared the simulated evaporative fraction (ET/P) to the observed (Figure 6). In  
 391 all three model configurations the KGE values tend to be higher for sites where the simulated  
 392 evaporative fraction closely matches the observed value.



393

394 **Figure 6.** Comparison of evaporative fraction for each model configuration across all sites. The  
 395 one-to-one line shows perfect correspondence with the observed values. Each point shows an  
 396 individual site, averaged over the simulation period. Points are colored by their respective  
 397 performance in terms of KGE of the latent heat at the half-hour timescale.

398 However, the SA configuration has a tendency to systematically underestimate total ET, while  
 399 the NN configurations tend to match the observed evaporative fraction. The NN1W  
 400 configuration shows more over-evaporation than NN2W, indicating that the introduction of soil  
 401 states allows the model to perform better in moisture limiting conditions. This soil moisture  
 402 feedback is the reason that the NN2W was able to perform better at daily and greater temporal  
 403 aggregations for the prediction of latent heat. The impacts of these changes in the long-term  
 404 evaporative fraction on the other terms of the water balance are shown in figure S3 of the  
 405 supporting materials.

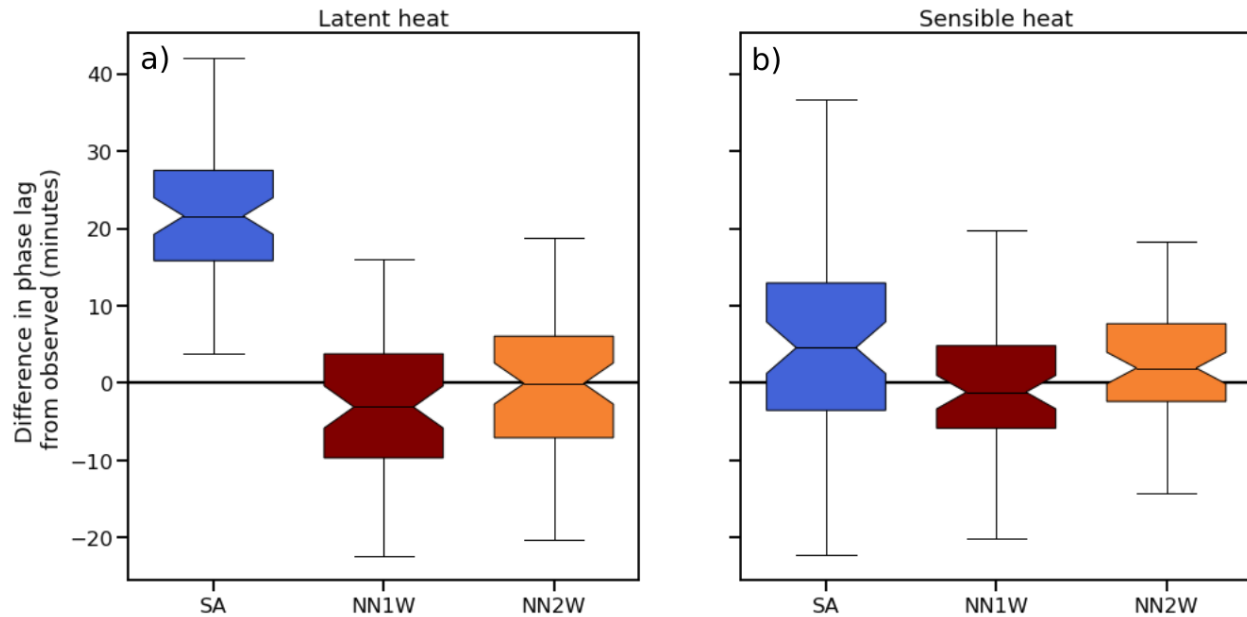
406 As noted when discussing Figure 5, we hypothesize that the NN-based simulations performed  
 407 better at the sub-daily timescale because of their improved ability to model the diurnal cycle in  
 408 the observations. We take the approach of Renner et al. (2019) by comparing the time lag in the  
 409 diurnal cycle between the turbulent heat fluxes and shortwave radiation. To compute this we  
 410 fitted a regression equation of the form:

$$411 \quad Q(t) = a_0 + a_1 SW(t) + a_2 \frac{dSW(t)}{dt} + \epsilon, \quad (1)$$

412 where  $Q$  is the turbulent heat flux,  $SW$  is the shortwave radiation,  $a_i$  are the coefficients of the  
 413 regression, and  $\epsilon$  is the residual term (Camuffo & Bernardi, 1982). Then, the phase lag can be  
 414 computed as

$$415 \quad \phi = \tan^{-1}(2\pi a_2 / a_1 n_d), \quad (2)$$

416 where  $n_d$  is the number of timesteps in a day (here, 48). We calculated this phase lag for each of  
 417 the simulation configurations and the observations. Figure 7 shows how each of the simulations  
 418 compare to the observed phase lag across all sites. For both latent and sensible heat we see that  
 419 the NN-based configurations are better able to capture the diurnal phase lag seen in the  
 420 observations, confirming our conclusion from Figure 5 that the improved sub-daily performance  
 421 of the NN-based configurations is due to better representation of the diurnal cycle.



422  
423 **Figure 7.** Difference in diurnal phase lag from observation. Positive values indicate that the  
424 simulated phase lag leads the observed phase lag.

#### 425 **4 Discussion**

426 Our analysis shows that the DL parameterizations were able to outperform the standalone  
427 simulations for both latent and sensible heat fluxes. Most of the bulk gains in performance from  
428 the NN-based configurations stemmed from drastic improvements at sites where the SA  
429 configuration performed poorly. This is important to note, since our SA simulations were  
430 calibrated at site (and included the calibration period in the evaluation), while all NN-based  
431 simulations were trained out of sample in both time and space. This indicates that our NN-based  
432 configurations would likely be better able to represent turbulent heat fluxes in regions without  
433 measurements, implying that deep learning may be suitable for regionalization applications.

434 Both of the NN-based configurations represented the diurnal phase lag between shortwave  
435 radiation and turbulent heat fluxes better than SA. Renner et al. (2020) explored the ability of the  
436 land surface models used in the PLUMBER experiments (Best et al., 2015) to reproduce the  
437 observed diurnal phase lag, finding similar deviations from the observed phase lag as our SA  
438 simulations. This indicates that the NN-based approach has been able to learn something that has  
439 not been codified in PBHMs, and could provide better insight into how turbulent heat fluxes are  
440 generated at the scales that FluxNet towers operate. It is difficult to definitively state why the  
441 NN-based simulations provided more accurate simulations than SA's process-based  
442 parameterizations. Even if the functional forms of the SA were correct, the model parameters  
443 may be difficult to determine. Zhao et al. (2019) were able to achieve good predictive  
444 performance out of a standalone (that is, not coupled to a larger model) machine-learning model  
445 that used a neural network to estimate the resistance term of the bulk transfer equations, and then  
446 computed the heat fluxes from the standard equations. Using such an approach would likely  
447 work well in the coupled setting as well.

448 We also found that the NN2W configuration maintained higher performance than either NN1W  
449 or SA at longer than daily timescales, as well as more accurately reproduced the observed long-

450 term evaporative fraction. This indicates that the synergy between the deep-learned  
451 parameterization and the soil-moisture state evolution in SUMMA was able to better capture the  
452 long-term dynamics than either a purely machine-learned or purely process-based approach. This  
453 lends credibility to our proposition that the synergy between data-driven and physics-based  
454 approaches will likely lead to better simulations than a rigid adherence to either one of the  
455 methods by themselves.

456 These performance gains came at the cost of drastically simplifying the way in which we  
457 represented evapotranspiration. The SA simulations partition the latent heat fluxes amongst the  
458 soil, snow, and vegetation domains separately, while the NN simulations were set up to only  
459 represent the latent heat as a bulk flux, whose withdrawals we set to be taken from each soil  
460 layer according to the root density in that layer. This leads to the SA simulations being able to  
461 represent a more diverse range of conditions. While this was not a problem for the NN  
462 simulations on average, we were able to identify two locations where our simplification to the  
463 way in which ET is taken from the soil led to poor performance. At US-WCr and US-AR2 both  
464 NN configurations underestimated ET, because the soil was too dry to meet evaporative demand  
465 for much of the time. At these two sites the NN simulations performed significantly worse than  
466 the SA simulations, indicating a clear failure mode of the neural network based approach. This  
467 shortcoming might be addressed by developing strategies that better partition the latent heat  
468 fluxes amongst the soil, snow, and vegetation domains. This would also allow for adding snow  
469 sublimation back in, reducing the number of modifications which must be made to SUMMA in  
470 order to run with an embedded neural network.

471 Other neural network architectures will likely lead to further performance improvements. Many  
472 recent studies that used neural networks to predict hydrologic systems have shown that Long-  
473 Short-Term-Memory (LSTM) networks are superior at learning timeseries behaviors compared  
474 to the methods used here (Feng et al., 2020; Frame et al., 2020; Jiang et al., 2020; Kratzert et al.,  
475 2018). Convolutional neural networks (CNN) have been used extensively to learn from spatially  
476 distributed fields (Geng & Wang, 2020; Kreyenberg et al., 2019; Liu & Wu, 2016; Pan et al.,  
477 2019). To take advantage of these specialized architectures in existing PBHMs like SUMMA  
478 will require the investment in tools and workflows. As of the time of writing, the FKB library  
479 only supports densely connected layers, and a few simple activation and loss functions.  
480 Implementing these layers in the FKB library, or some other framework that can be used to  
481 couple ML models with PBHMs, would open many possibilities for future research.  
482 Additionally, implementing more specialized activation functions and loss functions (such as  
483 NSE or KGE) will offer more flexibility for a wider range of applications.

484 Alongside better tools for incorporating machine learning into process-based models, the  
485 development and identification of workflows to perform machine and deep learning tasks will be  
486 necessary for wider adoption in the field. For instance, we initially trained the NN2W networks  
487 using the SA soil states, which were drastically different from the spun up states in the NN  
488 configurations. This led to almost identical performance in the NN1W and NN2W simulations,  
489 since the soil state information from the SA simulations was very different from what the  
490 network saw during training. Only after realizing this and training the NN2W on the states  
491 predicted by the NN1W simulations were we able to achieve better performance out of the  
492 NN2W simulations. Understanding whether there is a sort of iterative train-spinup-train

493 workflow that balances overfitting and provides representative training data will be important for  
494 future studies.

495 Similarly, it is unclear whether there would be significant difficulties in trying to calibrate either  
496 of the NN-based models in new basins like we did for the SA simulations. Particularly, we do  
497 not know if the output of the neural networks is sensitive to the values of the calibration  
498 parameters. Our decision to include the calibrated parameter values in the training of the NN-  
499 based configurations was to provide the same types of information to both optimization  
500 procedures. In future studies it may be worthwhile to explore whether these parameters are  
501 necessary, or how regionalization of data driven approaches should best be codified. It is also  
502 unclear whether our NN-based configurations are able to be calibrated efficiently for other  
503 processes such as streamflow.

504 Finally, model architectures that separate process parameterizations in as clean a way as possible  
505 will allow for more robust and rapid development of ML parameterizations of other processes.  
506 Building modular and general purpose ways to incorporate machine learning into process-based  
507 models will allow researchers to more efficiently evaluate different approaches. Exploring and  
508 answering these practical questions will likely lead to community accepted practices which can  
509 be adopted to accelerate research of other applications.

## 510 **5 Conclusions**

511 We have shown that coupling DL parameterizations for prediction of turbulent heat fluxes into a  
512 PBHM outperforms existing physically-based parameterizations while maintaining mass and  
513 energy balance. We were able to couple our neural networks into SUMMA in two different  
514 ways, which both showed significant performance improvements when performed out of sample  
515 over the at-site calibrated standalone SUMMA simulations. The one-way coupling (NN1W),  
516 despite being conceptually simpler and not taking any model states as inputs, was able to  
517 improve simulations almost as much as the more complex two-way coupling (NN2W) at the sub-  
518 daily timescale. Both of the new parameterizations better represent the observed diurnal cycles  
519 and NN2W was better able to represent the long-term evaporative fraction as well as both  
520 turbulent heat fluxes at longer than daily timescales. We found that NN1W was also able to  
521 accurately predict sensible heat fluxes at greater than daily timescales, indicating that even  
522 “simple” DL parameterizations show great promise for coupling into PBHMs.

523 While we consider our new parameterizations a step forward in incorporating ML techniques  
524 into traditional process-based modeling, we have only scratched the surface on many of the  
525 different avenues which will surely be explored. We used the simplest possible network  
526 architecture, a deep-dense network. For spatial applications we suspect that CNN layers will  
527 prove invaluable. Recurrent layers such as LSTMs have been dominant in the timeseries domain.  
528 More sophisticated architectures such as neural ordinary differential equations (Ramadhan et al.,  
529 2020) or those discovered through neural architecture search (Geng & Wang, 2020) are bound to  
530 be both more efficient and interpretable than our dense networks. The opportunities for  
531 incorporating and learning from ML-based models into the hydrologic sciences are virtually  
532 untapped. We believe that as the community builds tools and workflows around the existing ML  
533 ecosystems we will be able to unlock this potential.

534 **Acknowledgments, Samples, and Data**

535 We would like to thank Yifan Cheng and Yixin Mao for reading and commenting on an early  
 536 version of this manuscript. Their comments improved the clarity and framing of our work. The  
 537 code to process, configure, calibrate/train, run, and analyze the FluxNet data is available at  
 538 <https://doi.org/10.5281/zenodo.4300929>. The SUMMA model configuration for SA is available  
 539 at <https://doi.org/10.5281/zenodo.4300931>. The SUMMA model configuration for NN1W is  
 540 available at <https://doi.org/10.5281/zenodo.4300932>. The SUMMA model configuration for  
 541 NN2W is available at <https://doi.org/10.5281/zenodo.4300933>. We would like to acknowledge  
 542 high-performance computing support from Cheyenne (doi:10.5065/D6RX99HX) provided by  
 543 NCAR's Computational and Information Systems Laboratory, sponsored by the National Science  
 544 Foundation.

545

546 **References**

- 547 Ball, J. T., Woodrow, I. E., & Berry, J. A. (1987). A Model Predicting Stomatal Conductance and its  
 548 Contribution to the Control of Photosynthesis under Different Environmental Conditions. In J.  
 549 Biggins (Ed.), *Progress in Photosynthesis Research: Volume 4 Proceedings of the VIIth*  
 550 *International Congress on Photosynthesis Providence, Rhode Island, USA, August 10–15, 1986*  
 551 (pp. 221–224). Dordrecht: Springer Netherlands. [https://doi.org/10.1007/978-94-017-0519-6\\_48](https://doi.org/10.1007/978-94-017-0519-6_48)
- 552 Best, M. J., Abramowitz, G., Johnson, H. R., Pitman, A. J., Balsamo, G., Boone, A., et al. (2015). The  
 553 Plumbing of Land Surface Models: Benchmarking Model Performance. *Journal of*  
 554 *Hydrometeorology*, 16(3), 1425–1442. <https://doi.org/10.1175/JHM-D-14-0158.1>
- 555 Bonan, G. (2015). *Ecological Climatology: Concepts and Applications*. Cambridge University Press.
- 556 Brenowitz, N. D., & Bretherton, C. S. (2018). Prognostic Validation of a Neural Network Unified Physics  
 557 Parameterization. *Geophysical Research Letters*, 45(12), 6289–6298.  
 558 <https://doi.org/10.1029/2018GL078510>
- 559 Camuffo, D., & Bernardi, A. (1982). An observational study of heat fluxes and their relationships with  
 560 net radiation. *Boundary-Layer Meteorology*, 23(3), 359–368.  
 561 <https://doi.org/10.1007/BF00121121>
- 562 Chollet, F. (2015). Keras. Retrieved from <https://github.com/fchollet/keras>
- 563 Clark, M. P., Nijssen, B., Lundquist, J. D., Kavetski, D., Rupp, D. E., Woods, R. A., et al. (2015). A  
 564 unified approach for process-based hydrologic modeling: 1. Modeling concept: A unified

- 565 approach for process-based hydrologic modeling. *Water Resources Research*, 51(4), 2498–2514.  
566 <https://doi.org/10.1002/2015WR017198>
- 567 Dee, D. P., Uppala, S. M., Simmons, A. J., Berrisford, P., Poli, P., Kobayashi, S., et al. (2011). The ERA-  
568 Interim reanalysis: configuration and performance of the data assimilation system. *Quarterly*  
569 *Journal of the Royal Meteorological Society*, 137(656), 553–597. <https://doi.org/10.1002/qj.828>
- 570 Feng, D., Fang, K., & Shen, C. (2020). Enhancing streamflow forecast and extracting insights using long-  
571 short term memory networks with data integration at continental scales. *ArXiv:1912.08949 [Cs,*  
572 *Stat]*. Retrieved from <http://arxiv.org/abs/1912.08949>
- 573 Foken, T. (2008). The Energy Balance Closure Problem: An Overview. *Ecological Applications*, 18(6),  
574 1351–1367. <https://doi.org/10.1890/06-0922.1>
- 575 Frame, J., Nearing, G., Kratzert, F., & Rahman, M. (2020). *Post processing the U.S. National Water*  
576 *Model with a Long Short-Term Memory network* (preprint). EarthArXiv.  
577 <https://doi.org/10.31223/osf.io/4xhac>
- 578 Geng, Z., & Wang, Y. (2020). Automated design of a convolutional neural network with multi-scale  
579 filters for cost-efficient seismic data classification. *Nature Communications*, 11(1), 3311.  
580 <https://doi.org/10.1038/s41467-020-17123-6>
- 581 Hu, C., Wu, Q., Li, H., Jian, S., Li, N., & Lou, Z. (2018). Deep Learning with a Long Short-Term  
582 Memory Networks Approach for Rainfall-Runoff Simulation. *Water*, 10(11), 1543.  
583 <https://doi.org/10.3390/w10111543>
- 584 Jiang, S., Zheng, Y., & Solomatine, D. (2020). Improving AI System Awareness of Geoscience  
585 Knowledge: Symbiotic Integration of Physical Approaches and Deep Learning. *Geophysical*  
586 *Research Letters*, 47(13), e2020GL088229. <https://doi.org/10.1029/2020GL088229>
- 587 Jung, M., Reichstein, M., & Bondeau, A. (2009). Towards global empirical upscaling of FLUXNET eddy  
588 covariance observations: validation of a model tree ensemble approach using a biosphere model,  
589 13.

- 590 Kidston, J., Brümmer, C., Black, T. A., Morgenstern, K., Nesic, Z., McCaughey, J. H., & Barr, A. G.  
591 (2010). Energy Balance Closure Using Eddy Covariance Above Two Different Land Surfaces  
592 and Implications for CO<sub>2</sub> Flux Measurements. *Boundary-Layer Meteorology*, 136(2), 193–218.  
593 <https://doi.org/10.1007/s10546-010-9507-y>
- 594 Knoben, W. J. M., Freer, J. E., & Woods, R. A. (2019). Technical note: Inherent benchmark or not?  
595 Comparing Nash–Sutcliffe and Kling–Gupta efficiency scores. *Hydrology and Earth System*  
596 *Sciences*, 23(10), 4323–4331. <https://doi.org/10.5194/hess-23-4323-2019>
- 597 Kratzert, F., Klotz, D., Brenner, C., Schulz, K., & Herrnegger, M. (2018). Rainfall-Runoff modelling  
598 using Long-Short-Term-Memory (LSTM) networks. *Hydrology and Earth System Sciences*  
599 *Discussions*, 1–26. <https://doi.org/10.5194/hess-2018-247>
- 600 Kreyenberg, P. J., Bauser, H. H., & Roth, K. (2019). Velocity Field Estimation on Density-Driven Solute  
601 Transport With a Convolutional Neural Network. *Water Resources Research*, 55(8), 7275–7293.  
602 <https://doi.org/10.1029/2019WR024833>
- 603 Lathière, J., Hauglustaine, D. A., & Friend, A. D. (2006). Impact of climate variability and land use  
604 changes on global biogenic volatile organic compound emissions. *Atmos. Chem. Phys.*, 19.
- 605 Li, L., Wang, Y.-P., Yu, Q., Pak, B., Eamus, D., Yan, J., et al. (2012). Improving the responses of the  
606 Australian community land surface model (CABLE) to seasonal drought. *Journal of Geophysical*  
607 *Research: Biogeosciences*, 117(G4). <https://doi.org/10.1029/2012JG002038>
- 608 Liu, Y., & Wu, L. (2016). Geological Disaster Recognition on Optical Remote Sensing Images Using  
609 Deep Learning. *Procedia Computer Science*, 91, 566–575.  
610 <https://doi.org/10.1016/j.procs.2016.07.144>
- 611 Matott, L. S. (2017). OSTRICH: an Optimization Software Tool, Documentation and User’s Guide,  
612 Version 17.12.19. University at Buffalo Center for Computational Research. Retrieved from  
613 [www.eng.buffalo.edu/~lsmatott/Ostrich/OstrichMain.html](http://www.eng.buffalo.edu/~lsmatott/Ostrich/OstrichMain.html)
- 614 Moshe, Z., Metzger, A., Elidan, G., Kratzert, F., Nevo, S., & El-Yaniv, R. (2020). HydroNets: Leveraging  
615 River Structure for Hydrologic Modeling. Retrieved from <https://arxiv.org/abs/2007.00595v1>

- 616 Musselman, K. N., Clark, M. P., Liu, C., Ikeda, K., & Rasmussen, R. (2017). Slower snowmelt in a  
617 warmer world. *Nature Climate Change*, 7(3), 214–219. <https://doi.org/10.1038/nclimate3225>
- 618 Nearing, G. S., Kratzert, F., Sampson, A. K., Pelissier, C. S., Klotz, D., Frame, J. M., et al. (2020). What  
619 Role Does Hydrological Science Play in the Age of Machine Learning? *Water Resources*  
620 *Research*, e2020WR028091. <https://doi.org/10.1029/2020WR028091>
- 621 Niu, G.-Y., Yang, Z.-L., Mitchell, K. E., Chen, F., Ek, M. B., Barlage, M., et al. (2011). The community  
622 Noah land surface model with multiparameterization options (Noah-MP): 1. Model description  
623 and evaluation with local-scale measurements. *Journal of Geophysical Research: Atmospheres*,  
624 116(D12). <https://doi.org/10.1029/2010JD015139>
- 625 Ott, J., Pritchard, M., Best, N., Linstead, E., Curcic, M., & Baldi, P. (2020). A Fortran-Keras Deep  
626 Learning Bridge for Scientific Computing. *ArXiv:2004.10652 [Cs]*. Retrieved from  
627 <http://arxiv.org/abs/2004.10652>
- 628 Pan, B., Hsu, K., AghaKouchak, A., & Sorooshian, S. (2019). Improving Precipitation Estimation Using  
629 Convolutional Neural Network. *Water Resources Research*, 55(3), 2301–2321.  
630 <https://doi.org/10.1029/2018WR024090>
- 631 Pastorello, G., Trotta, C., Canfora, E., Chu, H., Christianson, D., Cheah, Y.-W., et al. (2020). The  
632 FLUXNET2015 dataset and the ONEFlux processing pipeline for eddy covariance data. *Scientific*  
633 *Data*, 7(1), 225. <https://doi.org/10.1038/s41597-020-0534-3>
- 634 Ramadhan, A., Marshall, J., Souza, A., Wagner, G. L., Ponnampati, M., & Rackauckas, C. (2020).  
635 Capturing missing physics in climate model parameterizations using neural differential equations.  
636 *ArXiv:2010.12559 [Physics]*. Retrieved from <http://arxiv.org/abs/2010.12559>
- 637 Rasp, S., Pritchard, M. S., & Gentine, P. (2018). Deep learning to represent subgrid processes in climate  
638 models. *Proceedings of the National Academy of Sciences*, 115(39), 9684–9689.  
639 <https://doi.org/10.1073/pnas.1810286115>
- 640 Renner, M., Brenner, C., Mallick, K., Wizemann, H.-D., Conte, L., Trebs, I., et al. (2019). Using phase  
641 lags to evaluate model biases in simulating the diurnal cycle of evapotranspiration: a case study in

- 642 Luxembourg. *Hydrology and Earth System Sciences*, 23(1), 515–535.  
643 <https://doi.org/10.5194/hess-23-515-2019>
- 644 Renner, M., Kleidon, A., Clark, M., Nijssen, B., Heidkamp, M., Best, M., & Abramowitz, G. (n.d.). How  
645 well can land-surface models represent the diurnal cycle of turbulent heat fluxes? *Journal of*  
646 *Hydrometeorology*, 1–56. <https://doi.org/10.1175/JHM-D-20-0034.1>
- 647 Shen, C. (2018). A Transdisciplinary Review of Deep Learning Research and Its Relevance for Water  
648 Resources Scientists. *Water Resources Research*, 54(11), 8558–8593.  
649 <https://doi.org/10.1029/2018WR022643>
- 650 Tolson, B. A., & Shoemaker, C. A. (2007). Dynamically dimensioned search algorithm for  
651 computationally efficient watershed model calibration. *Water Resources Research*, 43(1).  
652 <https://doi.org/10.1029/2005WR004723>
- 653 Tramontana, G., Jung, M., Schwalm, C. R., Ichii, K., Camps-Valls, G., Ráduly, B., et al. (2016).  
654 Predicting carbon dioxide and energy fluxes across global FLUXNET sites with regression  
655 algorithms. *Biogeosciences*, 13(14), 4291–4313. <https://doi.org/10.5194/bg-13-4291-2016>
- 656 Wilson, K., Goldstein, A., Falge, E., Aubinet, M., Baldocchi, D., Berbigier, P., et al. (2002). Energy  
657 balance closure at FLUXNET sites. *Agricultural and Forest Meteorology*, 113(1), 223–243.  
658 [https://doi.org/10.1016/S0168-1923\(02\)00109-0](https://doi.org/10.1016/S0168-1923(02)00109-0)
- 659 Zhao, W. L., Gentine, P., Reichstein, M., Zhang, Y., Zhou, S., Wen, Y., et al. (2019). Physics-  
660 Constrained Machine Learning of Evapotranspiration. *Geophysical Research Letters*, 46(24),  
661 14496–14507. <https://doi.org/10.1029/2019GL085291>

662